

Research Article

Electromagnetic Analysis and Experimental Validation of the LOFAR Radiation Patterns

Paola Di Ninni ¹, Pietro Bolli ¹, Fabio Paonessa ², Giuseppe Pupillo ³,
Giuseppe Virone ² and Stefan J. Wijnholds⁴

¹Osservatorio Astrofisico di Arcetri, Istituto Nazionale di Astrofisica, Florence 50125, Italy

²Istituto di Elettronica e di Ingegneria dell'Informazione e delle Telecomunicazioni, Consiglio Nazionale delle Ricerche, Turin 10129, Italy

³Istituto di Radioastronomia, Istituto Nazionale di Astrofisica, Bologna 40129, Italy

⁴Netherlands Institute for Radio Astronomy, Dwingeloo, 7991 PD, Netherlands

Correspondence should be addressed to Pietro Bolli; pbolli@arcetri.inaf.it

Received 14 September 2018; Accepted 29 October 2018; Published 27 January 2019

Academic Editor: Claudio Gennarelli

Copyright © 2019 Paola Di Ninni et al. This is an open access article distributed under the Creative Commons Attribution License, which permits unrestricted use, distribution, and reproduction in any medium, provided the original work is properly cited.

Low-frequency (<300 MHz) aperture array systems are one of the new trends in modern radio astronomy. Among the challenges they pose, the instrumental calibration is a key aspect requiring an accurate and reliable model of each element of such electrically large array. A full-wave electromagnetic analysis has been carried out for the lower frequency (30–80 MHz) array of the low frequency array (LOFAR) radio telescope taking into account the presence of soil ground, the mutual coupling between the antennas and the relevant receiver impedance loading effects. The impact of mutual coupling effects on the embedded element and array patterns is assessed for two subarray configurations with different degrees of sparseness. A simplistic array factor approach has been implemented as well to determine the accuracy in the antenna pattern evaluation with respect to the full-wave approach. Finally, results from an experimental campaign conducted by means of a micro hexacopter system show the reliability of the developed array numerical model.

1. Introduction

Since approximately two decades, radio astronomers are investing significant resources in studying and developing aperture array systems for radio astronomical observations. Aperture array technology exploits digital beamforming to steer the array beam towards the celestial sources. In order to have enough collecting area and high angular resolution, the array is composed of a multitude of small antennas spread over large distances. For instance, the low frequency aperture array (LFAA) subsystem of the square kilometre array (SKA) [1], the largest radio telescope ever built, will be composed of more than 130.000 antennas operating between 50 and 350 MHz. ASTRON, the Netherlands Institute for Radio Astronomy, inaugurated the low frequency array (LOFAR) in 2010 [2]. LOFAR is a pathfinder for the

SKA and is nowadays a world-class facility for astronomical research, with seven partner countries in Europe. It consists of 38 stations spread in the Netherlands and 13 deployed in other European countries. All stations include two different antenna types (see Figure 1): high-band antennas (HBA) working in the 120–240 MHz frequency range and low band antennas (LBA) operating between 30 and 80 MHz. The aperture array characteristics of the LBA system are conceptually similar to the LFAA planned for SKA. Therefore, the LBA array is widely used as an appropriate test bed to acquire experience in view of the SKA. In this perspective, the modelling activity on the LBA array, which is the focus of this paper, provides useful guidance for what can be expected for SKA.

The adopted antenna distribution for LBA array is a sparse random configuration of 96 antennas [2] divided in



FIGURE 1: (a) A LOFAR station composed by two regular HBA arrays and the random LBA array. (b) Zoom on the individual LBA.

two different subarrays called LBA-outer and LBA-inner, the former being sparser than the latter. The randomized positions of the antennas in both LBA subarrays not only assure a smoothness of the station pattern without grating lobes [3, 4] but also cause a significant diversity in the responses of each individual antenna due to mutual coupling effects. As a result, the array calibration becomes quite challenging as every antenna response needs to be evaluated individually [5]. This is further complicated by the strong dependence of the embedded patterns on the receiver impedance, especially at the resonance frequency as discussed in [6].

The current LOFAR data reduction pipeline assumes very simple and identical embedded-element patterns. Therefore, an accurate characterization of the antenna patterns by including the effect of soil ground, the mutual coupling effects, and the receiver impedance is expected to improve the quality of the astronomical data, especially for the LBA-inner array where the antenna coupling levels are higher. Fortunately, the availability of both powerful hardware resources and reliable computational electromagnetic tools nowadays make it possible to accurately simulate antenna patterns in a complex environment with a full-wave approach.

In this paper, we conduct a rigorous full-wave electromagnetic analysis of the LBA subarrays taking into account geometrical and electrical aspects of the arrays. Such results are compared to the present LOFAR calibration model (i.e., array factor multiplied by the isolated element pattern). The objective of this comparison is both to quantify the importance of the presented modelling approach and to assess its actual necessity in the sparse array scenario.

Furthermore, we validate the LBA array electromagnetic model using experimental data obtained during a measurement campaign performed in 2016 with an unmanned aerial vehicle (UAV) system described in [7]. This campaign has been already successfully used to characterize the LBA-inner array near-field (NF) pattern [8]. The novelty of this contribution is to show the agreement of the measured radiation patterns with the far-field (FF) numerical analysis.

The paper is organized as follows: the description of the LBA configuration and the model of a receiving array loaded by a receiver chain network are described in Sections 2 and 3, respectively. The numerical results for the LBA-inner and LBA-outer arrays are reported in Section 4 for the FF regime, whereas the measurement results obtained with the UAV

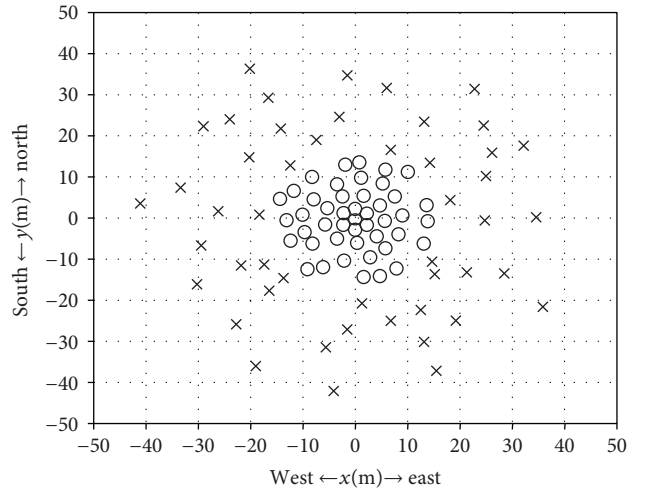


FIGURE 2: LBA geometry: the inner antenna distribution is the LBA-inner array (circles) and the outermost distribution is the LBA-outer array (crosses).

system are compared to simulations in Section 5. Finally, Section 6 draws the conclusions.

2. Low-Band Antenna Configurations

Low-band antennas are arranged in randomly perturbed rings with exponentially increasing radii (see Figure 2). The LBA-inner array is composed of 46 dual-polarized antennas distributed within a 30 m circle (plus two outer antennas used for calibration purposes, not shown in Figure 2), while the LBA-outer array consists of 48 dual-polarized antennas distributed in an annulus with a 30 m inner diameter and a 85 m outer diameter.

The antennas of the two subarrays are distributed with a different degree of sparseness and of randomization. The array sparseness is defined on the basis of the ratio between the averaged spacing (d) and the wavelength (λ). A threshold level of d/λ separates a dense array regime ($d/\lambda < 0.5$) from a sparse array regime ($d/\lambda > 0.5$) [9]. For each subarray, d is evaluated as the mean of the distances between each antenna and the nearest antenna within the subarray. The average values and their standard deviation turn out to be 3.4 ± 0.6 m and 7.3 ± 1.9 m for LBA-inner and LBA-outer,

TABLE 1: Array sparseness in terms of d/λ for LBA-inner and LBA-outer in the operating frequency band.

Frequency (MHz)	LBA-inner d/λ	LBA-outer d/λ
32	0.4	0.8
44	0.5	1.1
57	0.6	1.4
70	0.8	1.7

respectively. The d/λ ratios for the two LBA subarrays within the operating frequency range are reported in Table 1 (the frequencies are chosen to match those used in the UAV measurement campaign). The d/λ ratios show that the LBA-inner array can be considered a dense array for the frequencies below 44 MHz, while it behaves as a sparse array for frequencies larger than 44 MHz; the LBA-outer array is instead a sparse array for all operating frequencies.

As far as randomization is concerned, the LBA-outer array can be considered fully randomized while the LBA-inner array shows some regular features for the central area as evident from Figure 2.

The two subarrays are composed of identical receiving elements that cover the 30–80 MHz operating frequency bandwidth. Each element consists of two perpendicular inverted V-shaped dipole antennas sensitive to two orthogonal linear polarizations and is placed on a metallic wire mesh ground plane of $3 \times 3 \text{ m}^2$. The two dipoles are oriented at 45° with respect to the cardinal directions. Two low-noise amplifiers (LNA), enclosed in the black package at the antenna feeding point (see Figure 1(b)), increase the received signal levels before they are transported to the station cabinets through two coaxial cables [10].

3. Modelling of the Receiving Array

Due to the nonreciprocity of the amplifiers connected to the antennas, the LBA array electromagnetic characterization is conducted in receiving mode; therefore, the formulation in this paper is presented accordingly. A N -port equivalent Thévenin circuit [11] is employed to represent the receiving array system.

For the equivalent circuit in Figure 3, the voltages at the terminations of the receivers can be described in matrix form. Using this formulation, the column vector \mathbf{V}_r in equation (1) contains the N voltages at the terminations of the receivers and is described as follows:

$$\mathbf{V}_r = \mathbf{Z}_r (\mathbf{Z}_a + \mathbf{Z}_r)^{-1} \mathbf{V}_{oc}, \quad (1)$$

where \mathbf{Z}_r is a diagonal matrix accounting for the impedance of the receivers (which are not coupled to each other), \mathbf{Z}_a is the (full) array impedance matrix, and \mathbf{V}_{oc} is a column vector with the open-circuit voltages at the antenna terminals. Since the antennas are embedded in an array, the array impedance matrix accounts for the mutual coupling between the elements.

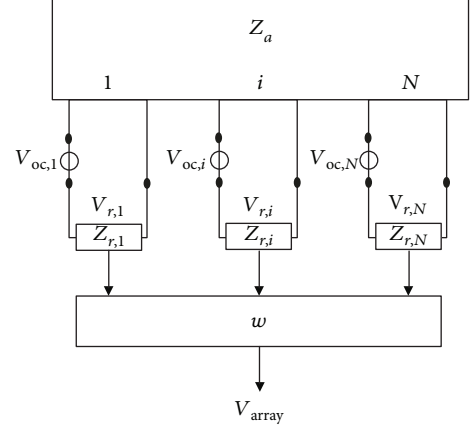


FIGURE 3: Thévenin circuit block diagram for a receiving array composed by N receiving ports and the output of the beamforming network.

It should be noted that V_r and V_{oc} depend on the observation direction. However, for the sake of simplicity, the dependence on the direction coordinates will be understood throughout the formulation. The i th component of the open-circuit voltage vector can be written as the scalar product between the incident electric field \mathbf{E}_{inc} (arbitrary polarized) and the receiving antenna effective length \mathbf{h}^i :

$$V_{oc}^i = \mathbf{E}_{inc} \cdot \mathbf{h}^i. \quad (2)$$

Exploiting the reciprocity principle, the antenna effective length can be deduced from the radiation electric field \mathbf{E}^i emitted by each single antenna through the following formula [12]:

$$\mathbf{E}^i = j \frac{Z}{2\lambda} \frac{e^{-jkr}}{4\pi r} I^i \mathbf{h}^i, \quad (3)$$

where r is the distance from the reference center, Z is the propagation medium impedance, λ is the receiving wavelength, k is the wavenumber, and I^i is the excited current at the antenna terminals.

Finally, the voltage at the output of the receiver network (V_{array}) is obtained as a weighted superposition (beamforming) of the voltage V_r induced at the terminations of the receiver devices [13]:

$$V_{array} = \mathbf{w}^T \mathbf{V}_r, \quad (4)$$

where \mathbf{w}^T is the transpose of the complex column vector composed of the N weights. This vector takes into account the gains of the receivers, the calibration coefficients, and the phases assigned to each single antenna to steer the array beam towards a specific direction.

To summarize, the formulation reported here allows to characterize the element and array pattern in loaded conditions starting from (i) the open-circuits embedded element patterns, (ii) the array impedance matrix, and (iii) the impedances of the receivers.

4. EM Analysis of the LBA Subarrays

Results presented in this paper are based on simulated data in the FF regime using FEKO, a commercial full-wave electromagnetic software package. Both LBA subarray geometries have been simulated separately based on their actual geometry and neglecting possible mutual coupling between the two subarrays. This latter assumption is made to not significantly increase the simulation computational time and has been validated by the experimental verification discussed in Section 5.

Each dual-polarized element has been simulated using two discrete ports. The size N introduced in Section 3 refers therefore to the total port number including both polarizations. A finite metallic grid under each element has been modelled by a $3 \times 3 \text{ m}^2$ solid rectangle of perfect electric conductor. Then, a semi-infinite dielectric layer (relative electric permittivity equal to 3 and conductivity equal to 0.01 S/m) is used to model the terrain.

The array impedance matrix has also been evaluated using FEKO. The LNA input impedances have been evaluated starting from the measured amplifier scattering parameters and considered identical for all elements: $(16.2-j341.0) \Omega$, $(5.6-j236.7) \Omega$, $(17.0-j215.3) \Omega$, and $(2.8-j137.2) \Omega$ at the four frequencies, respectively.

In the following analysis, a unity incident plane wave with a linear polarization aligned to the copolar component of the ports oriented along the north-east direction is adopted. The embedded element patterns are evaluated as the voltages V_r and they are referred to EEPs, while the resulting array beam patterns are evaluated as the voltage V_{array} .

Besides the rigorous full-wave analysis, the antenna pattern has also been computed under mutual coupling-free conditions by modelling only one dual-polarized antenna above the finite metallic rectangle and the semi-infinite soil ground. This approach results in an isolated element pattern, indicated as IEP. In this simplified case, the array factor has been used to evaluate the resulting array beam.

In the following analysis, the linear differences between full-wave and simplified patterns are used to quantify the agreement between the two approaches. Such figure of merit allows to de-emphasize possible spikes present in correspondence of the nulls of the array patterns [14].

4.1. Coupling Coefficients Results. A simple characterization of the mutual coupling in an array can be obtained by the analysis of the scattering matrix of the array. The scattering matrix assumes that all antennas are closed with matched loads. Therefore, in order to take into account highly mismatched receiver impedances, a column vector introduced in [6] (see equation (2) in that paper) is employed here. This vector represents the power waves reflected by $N-1$ receivers connected to the passive antennas when a specific antenna is excited. This quantity can be used to evaluate the amount of coupling between different pairs of antennas.

Figure 4 shows the coupling coefficients between all possible pairs of antennas both for LBA-outer (red dots) and LBA-inner arrays (black dots). The coupling is given as a function of distance between the antennas and results in a decreasing curve with distance. The LBA-inner array being

more compact than the LBA-outer array, the overall coupling for the first subarray is definitively higher than for the latter. A frequency dependence of the coupling level is also clearly visible, which is related to the antenna mismatch; in particular, at 57 MHz, the coupling level is higher than at other frequencies, since the antennas are better matched.

4.2. Discussion on the Element Patterns. The effects of mutual coupling on the FF embedded element patterns composing both the LBA-outer and LBA-inner subarrays are discussed in this subsection. Figures 5 and 6 show the patterns along the E-plane for the LBA-outer and LBA-inner configurations (polar angle between -60° and 60°), respectively. For each frequency and for each subarray, the results for the embedded element pattern analysis are organized in two panels. The upper panel shows a grey shading for the EEP distribution within one standard deviation, a black curve for the averaged EEPs (indicated as $\overline{\text{EEP}}$) and a grey curve for the IEP. Due to the resonance matching properties of the LBA dipoles with their amplifiers (see [6]), the pattern absolute levels turn out to be significantly frequency dependent. Therefore, in order to give a clear picture at all frequencies of the EEPs and IEP behavior, the patterns have been normalized to their maxima.

The bottom panel shows two curves: one, indicated as std is the normalized standard deviation of the EEPs distribution, while the other, ε (IEP, $\overline{\text{EEP}}$) is the difference between the isolated element pattern and the mean of the embedded element patterns. Both curves are computed on linear scales. The normalized standard deviation gives an idea of the level of diversity between the embedded element responses (which is related to the level of coupling and to the array irregularity), while the difference ε (IEP, $\overline{\text{EEP}}$) represents how well the isolated antenna pattern can be described as the average element response.

At 32, 44, and 70 MHz, the normalized standard deviation reported in Figure 5 shows that the variations between the LBA-outer embedded element patterns is so low that the shading turns out to be quite indiscernible from the $\overline{\text{EEP}}$ curve over the whole considered observation angle range. This is clearly visible from the black curves in the bottom panels where the normalized standard deviation is almost constantly lower than 3%. These results can be attributed to the sparse configuration of LBA-outer elements, which mitigates the mutual coupling effects. At 57 MHz, the resonance phenomenon due to the loaded antenna system [6] causes a magnification of the mutual coupling effect that is distinctly visible in Figure 5(c), where the normalized standard deviation increases to 5%.

Far from the resonance frequency, the $\overline{\text{EEP}}$ and the IEP curves are almost completely superimposed on each other (see the grey curves in the bottom panels). This suggests that the mutual coupling effects are almost completely negligible in the LBA-outer array, and therefore, a simpler mutual coupling-free approach produces quite accurate results that differ less than 1% from the full-wave analysis. At 57 MHz, the difference doubles (see the bottom panel of Figure 5(c)) for the aforementioned reasons.

Unlike the LBA-outer array, the upper and bottom panels of Figure 6 show that for the LBA-inner array, the variations

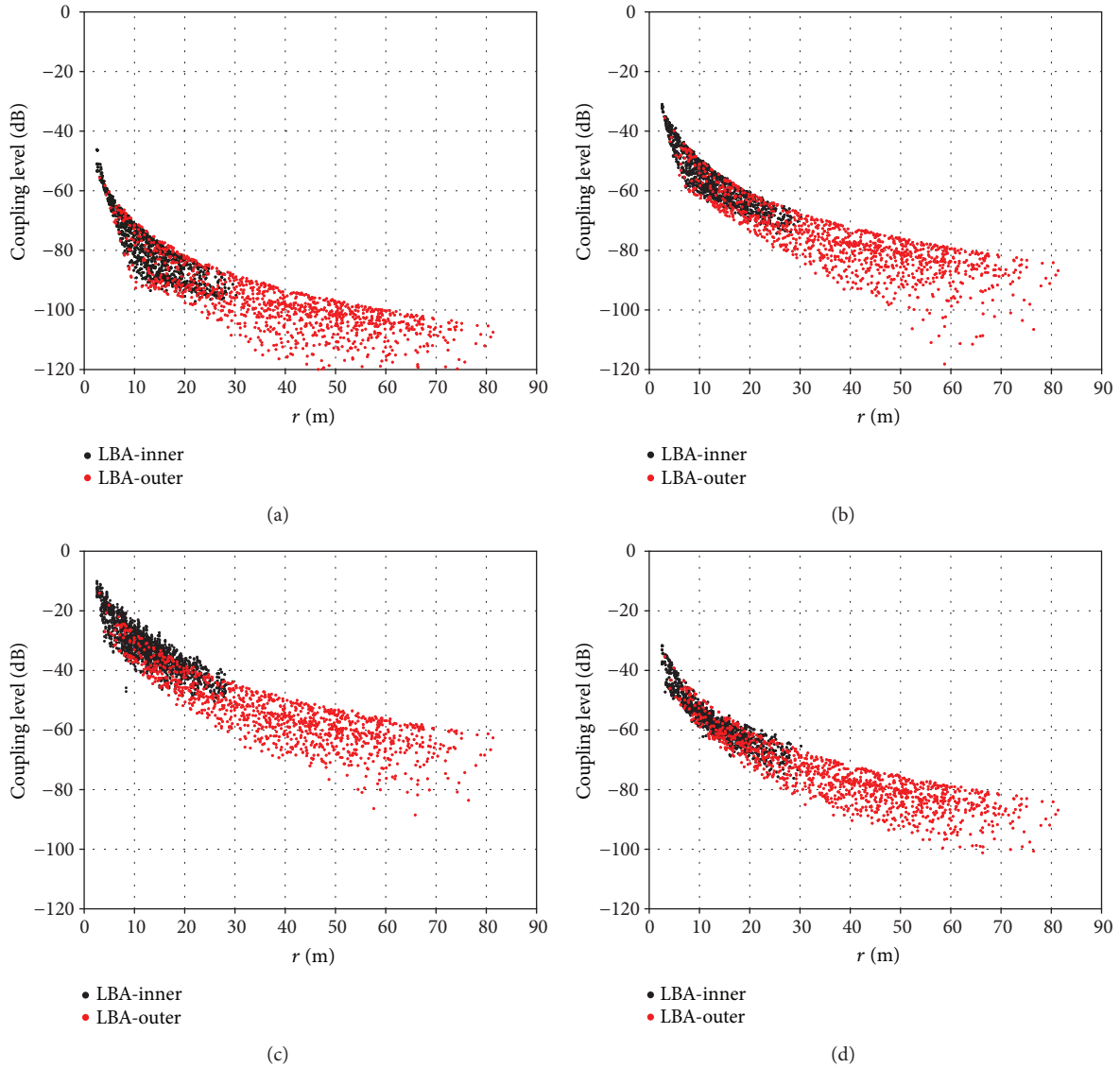


FIGURE 4: Coupling level for all possible distances between two antennas for LBA-outer (red points) and LBA-inner (black points) at different frequencies: (a) 32, (b) 44, (c) 57, and (d) 70 MHz.

between the embedded patterns are more significant with a normalized standard deviation between 6% and 12% (at 32, 44, and 70 MHz) and reaching levels as high as 20% at 57 MHz. This larger difference between antennas can be attributed to a less-randomized antenna distribution and to a higher mutual coupling due to the closer spacing. The stronger coupling effects are also visible in the difference between $\overline{\text{IEP}}$ and IEP curves even if with some peculiarities: at 32 MHz, the difference is comparable to the LBA-outer case (below 1%), while at the two central frequencies (44 and 57 MHz), it increases at 6%. However, the highest difference occurs at 70 MHz with 9% discrepancy.

4.3. Discussion on the Array Patterns. In this subsection, the embedded voltages evaluated above are summed together to produce the array patterns. These are computed by assuming that the weights in vector \mathbf{w} in equation (4) for the ports aligned to the north-east direction are all unity. This

equiphase feeding scheme produces a main beam pointing towards the zenith direction.

The simulated normalized array patterns are shown in Figures 7 and 8 along the E-plane (polar angle between -45° and 45°) for the LBA-outer and LBA-inner arrays, respectively. The corresponding array patterns computed by using the array factor approach is plotted as well. An additional panel shows the linear difference between the array patterns computed with the full-wave approach and the simplified one. The frequencies are again 32, 44, 57, and 70 MHz.

The discrepancy of the simplified approach from the rigorous full-wave analysis of the LBA-inner and LBA-outer arrays is highlighted in Table 2, which reports the maxima of the linear differences for the array patterns. It also includes the case of the array pattern steered to 25° zenith angle to evaluate the differences between the two approaches in an off-axis condition.

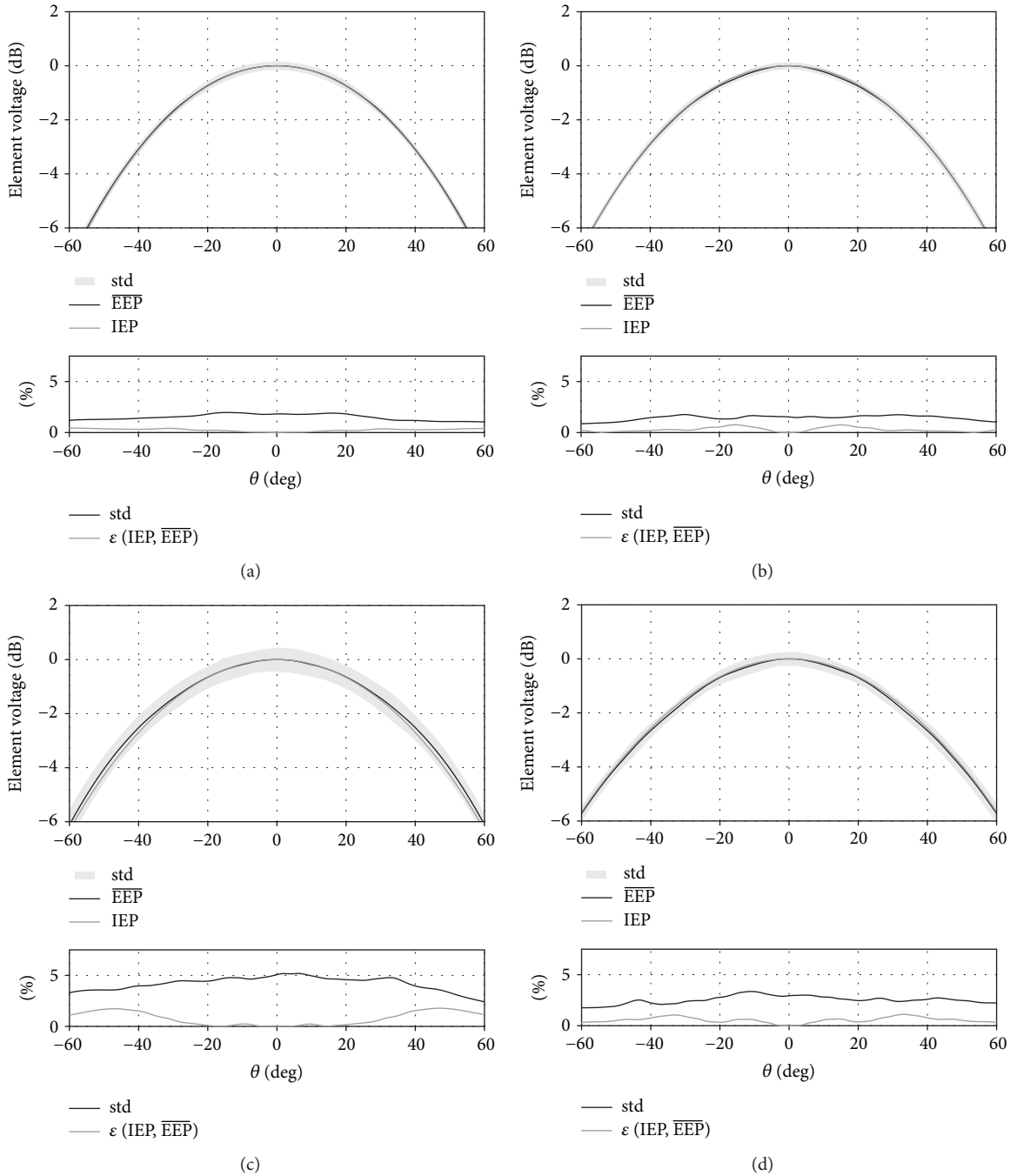


FIGURE 5: Normalized LBA-outer single element voltages at different frequencies: (a) 32, (b) 44, (c) 57, and (d) 70 MHz. Panels (a) and (b) show the embedded element pattern distribution (grey shading), their average (black curve), and the isolated element pattern (grey curve). Panels (c) and (d) show the normalized std distribution of the embedded element patterns (black curve) and the (percent) differences between the mean of the embedded element pattern and the isolated element pattern (grey curve).

The randomized distribution ensures that grating lobes are absent, as expected, and side lobes are always below -12 dB from the array peak. The overall agreement for the LBA-outer array (Figure 7) confirms the low mutual coupling already seen for the embedded patterns. The differences between the two curves do not exceed the error of 1% (corresponding to 0.1 dB) at 32 and 44 MHz, whereas the difference increases to 1.4% at 70 MHz and around 2% at 57 MHz.

On the other hand, the LBA-inner array patterns (Figure 8) indicate that the isolated antenna pattern produces less accurate results reaching difference up to 3% (corresponding to 0.25 dB) within the visible observation angle region at 32 and 44 MHz. At 57 and 70 MHz, such discrepancy increases to 7% and 5%, respectively.

In the LBA-outer array case, for every frequency, the accuracy levels for the array patterns are very similar to those computed for the embedded patterns. Vice-versa, in the

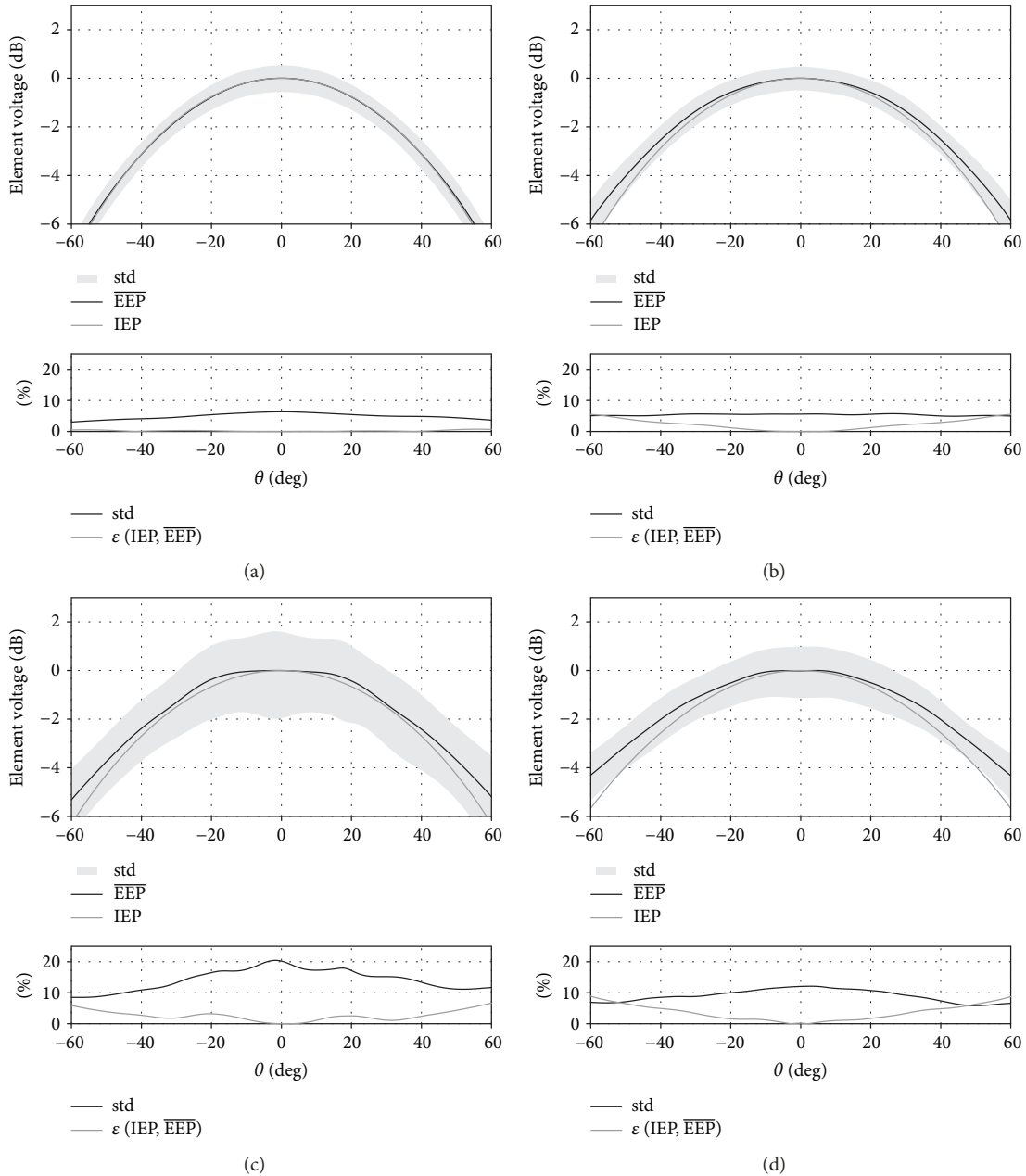


FIGURE 6: Normalized LBA-inner single element voltages at different frequencies: (a) 32, (b) 44, (c) 57, and (d) 70 MHz. The organization of the subplots is the same as in Figure 5.

LBA-inner array, it is not possible to identify a correspondence between embedded and array accuracies. This is likely due to the stronger mutual coupling and the random combination of the embedded patterns.

5. Experimental Validation of the LBA Subarrays EM Models

An intensive experimental characterization of a LOFAR station (CS302, located in Exloo, the Netherlands) was performed in 2016 by means of an UAV-mounted probe [6, 8]. This technology has been employed successfully to validate the electromagnetic model of several low-frequency aperture array systems [15, 16]. Both a radio frequency

transmitter connected to a 2 m long dipole and a differential global positioning system (GPS) were installed on the UAV. Such a flying test source performed several flights above the LOFAR telescope.

The experimental data recorded for the LBA-inner array was for only 40 of the 46 antennas composing the array; for this reason, the EM model used for the validation simulated all 46 antennas but left out (weight equal to zero) the missing antennas in the array pattern computation. As far as the LBA-outer array is concerned, all 48 elements were acquired during the campaign. For both subarrays, the ports aligned along the north-east direction have been considered. A flight along the north-east direction with a constant height of 300 m has been selected for the LBA-inner array, while the

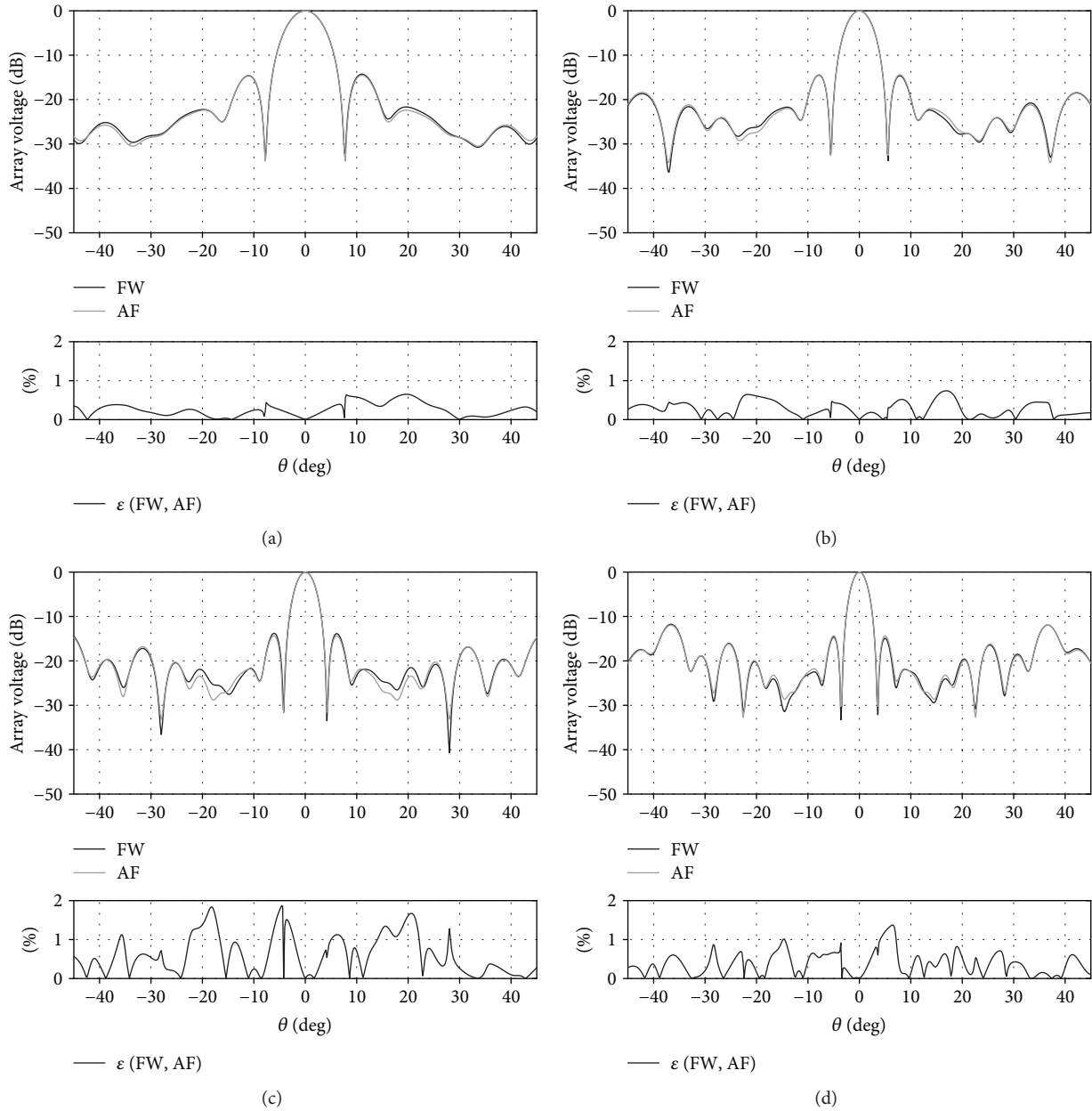


FIGURE 7: LBA-outer array voltages at different frequencies: (a) 32, (b) 44, (c) 57, and (d) 70 MHz. Panels (a) and (b) show the full-wave array pattern computed with the embedded element patterns (black curve, FW) and the array pattern based on the array factor (grey curve, AF). Panels (c) and (d) show the (percent) differences between the two array patterns.

only available UAV flight for the LBA-outer array was performed at a height of 100 m.

It is worthwhile emphasizing that for the LBA-inner array, the UAV trajectory is quite close to the FF region boundary (being 265 and 420 m at 44 and 70 MHz, respectively). On the contrary, the UAV was not able to reach the FF region of the LBA-outer array, the FF boundary being equal to 2100 m (44 MHz) and 3300 m (70 MHz).

The selected beamforming strategy to combine the measured embedded element patterns consists in the phase and amplitude equalization with the UAV located above the central element of the array [15]. Furthermore, the measured array patterns have been deconvolved, using

the Friis formula, for the distance between the array and the UAV and for the transmitting dipole pattern (see [7] for more details on the deconvolution procedure). According to the procedure applied for the experimental data, the numerical embedded patterns have been equalized at the zenith direction.

Figure 9 shows the normalized simulated and measured array patterns between observation angles of -45° and $+45^\circ$ in the top panels and the linear differences in the bottom panels. The array patterns in Figure 9 refer to the LBA-inner array (left column) and the LBA-outer array (right column). Patterns are plotted in the E-plane at the measured frequencies of 44, 57, and 70 MHz.

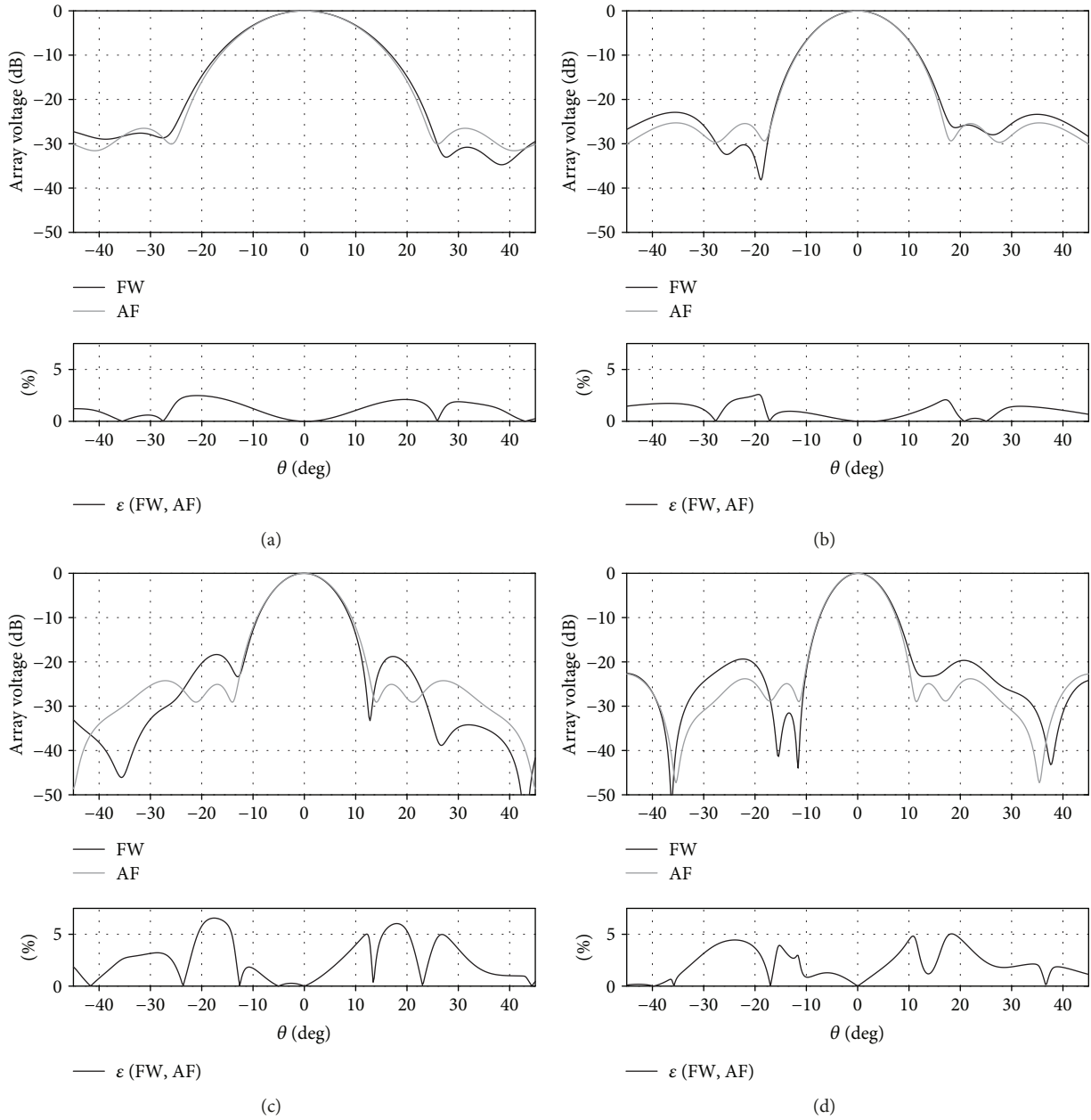


FIGURE 8: LBA-inner array voltages at different frequencies: (a) 32, (b) 44, (c) 57, and (d) 70 MHz. The organization of the subplots is the same as in Figure 7.

TABLE 2: Maxima of the linear differences between full-wave and array factor patterns. Values are given for different frequencies, subarrays, and pointing directions (0° and 25° zenith angle).

LBA	Pointing direction	Max ε (FW, AF) (%)			
		32 MHz	44 MHz	57 MHz	70 MHz
LBA-outer	0°	0.7	0.7	1.9	1.4
	25°	0.7	0.9	2.3	1.4
LBA-inner	0°	2.5	2.6	6.6	5.0
	25°	2.9	3.1	7.0	4.7

At all frequencies, the measured and simulated LBA-inner array patterns show an excellent agreement. At 44 and 70 MHz, the maximum of the differences is 1.5% and 2% (Figures 9(a) and 9(e)), respectively, whereas at 57 MHz, such difference reaches 4% (Figure 9(c)). The frequency of 57 MHz turns out to be the least accurate, which is due to the stronger dependence on the receiver impedance, and therefore, some inaccuracies in that value affect the simulated pattern response. The dependence of the simulated patterns from the receiver impedance is further discussed at the end of this section.

A larger disagreement is present for the LBA-outer array where the maximum of the difference grows up to 10%–20% depending on the frequency (Figures 9(b), 9(d), and 9(f)).

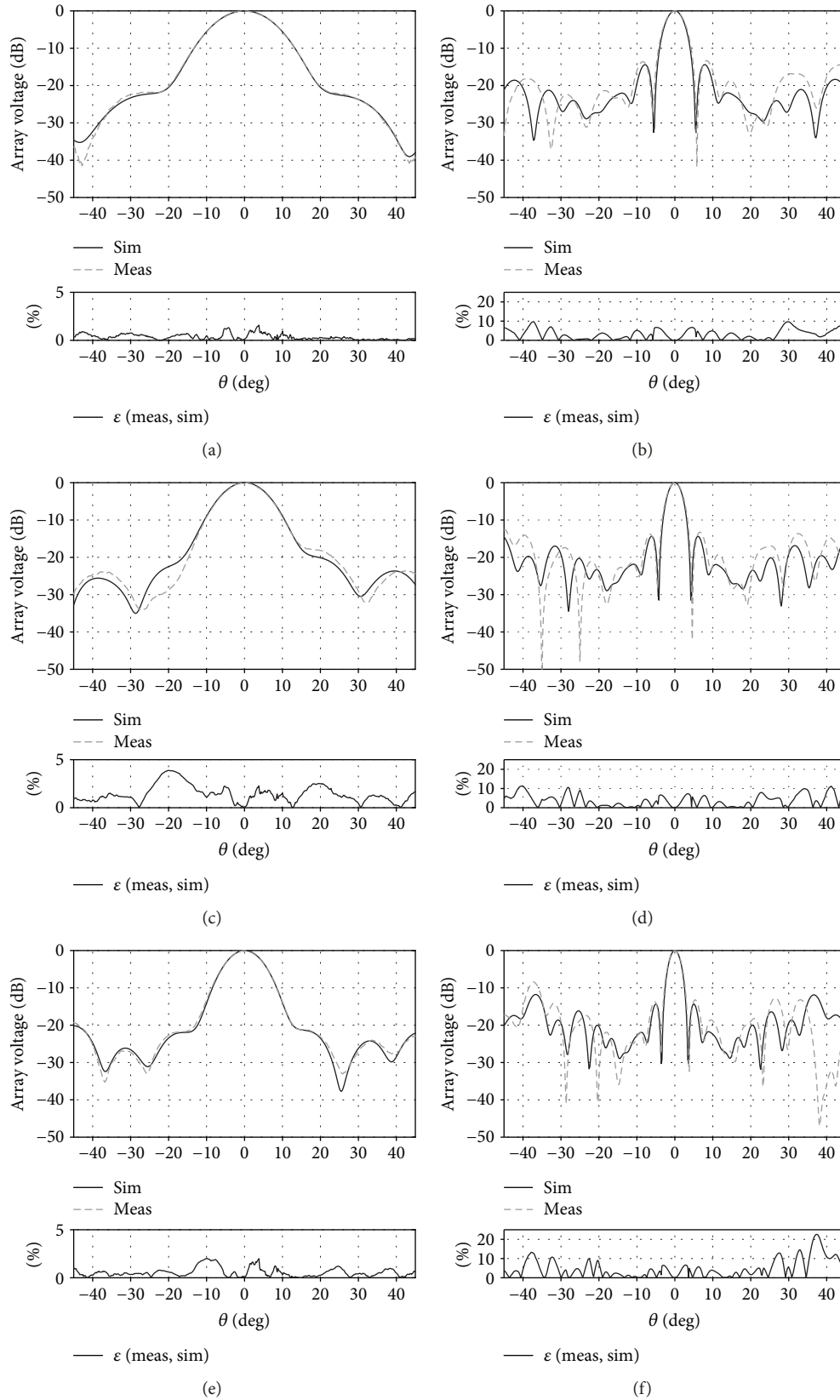


FIGURE 9: Measured and simulated array voltage at different frequencies for LBA-inner (a, c, e) and LBA-outer (b, d, f) arrays: (a, b) 44, (c, d) 57, and (e, f) 70 MHz. The top graphs of each panel show the normalized array pattern computed through measurements (grey dashed curve) and simulations (black continuous curve). The bottom graphs of panel show the (percent) differences between the two array patterns.

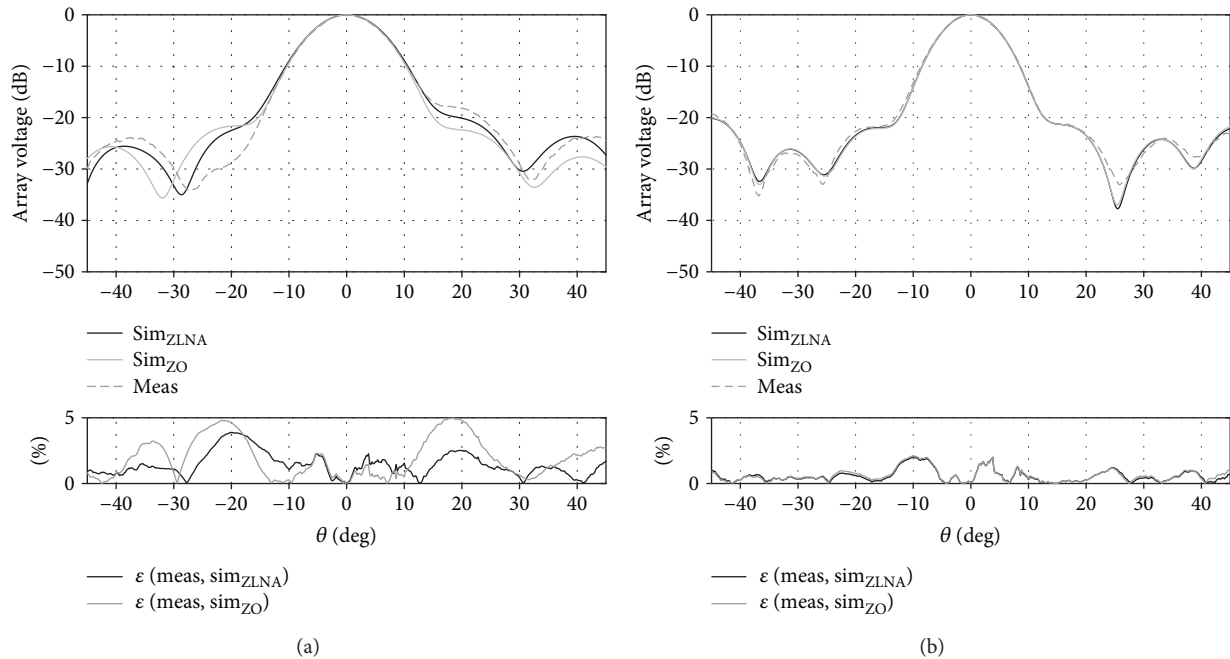


FIGURE 10: Measured and simulated array voltages at different loading conditions for LBA-inner array. Frequencies: (a) 57 and (b) 70 MHz. The top graphs show the array pattern computed through measurements (grey dashed curve), simulations loaded on the nominal LNA impedance (black continuous curve), and simulations loaded on $50\ \Omega$ (grey continuous curve). The bottom graphs show the linear differences between the measured and the two simulated patterns.

Such discrepancy between numerical and experimental analysis is due, as mentioned before, to the fact that the experimental patterns are measured very far from the FF region. This results confirms that for measurements performed in the NF region, the approach proposed in [8] with the simulations computed in NF is the correct strategy for the comparison.

Figure 9(c) suggests that an important condition to compare successfully the experimental and the simulated FF patterns, at the resonance frequency, is to consider the antennas loaded with the correct receiver impedance. In this respect, Figure 10(a) shows, for the LBA-inner array, the measured pattern at 57 MHz compared to two simulated patterns obtained with different LNA impedance values: standard $50\ \Omega$ and measured impedance (see Section 4). The simulated patterns turn out to be quite sensitive to the receiver impedance. Furthermore, the bottom panel of Figure 10(a) highlights that a better agreement with the measured data is reached when the antennas are simulated with the measured impedance (averaged difference 1.4%) rather than with $50\ \Omega$ (2%). On the contrary, at 70 MHz the antenna-receiver system is far from the resonance condition, and the two simulated array patterns almost overlap with an averaged discrepancy of only 0.6% (see Figure 10(b)).

6. Conclusions

A deep investigation of the array performance including mutual coupling and receiver impedance is an important step to improve the observation capabilities of an aperture array system. The rigorous approach defined in this contribution

for LOFAR can be considered a valid guideline that could be applied to other aperture array systems, such as the LFAA stations of SKA.

The proven reliability of the electromagnetic model permits to investigate and quantify the mutual coupling effect on the overall performance for two array configurations featuring different levels of sparseness. The mutual coupling has been evaluated by comparing the antenna patterns computed by a rigorous analysis and a simplified one based on an isolated antenna analysis.

Except for the resonance frequency, the LBA-outer array analysis shows quite a negligible difference between a mutual coupling-free approach and a full-wave analysis. As expected, the LBA-inner array is characterized by stronger mutual coupling between the antennas, which compromises the accuracy level reachable by using the isolated approach. Therefore, depending on the scientific requirements of the astronomical observation, the simplified approach may be inappropriate to model the antenna responses.

Finally, some measured results performed with a UAV system show an excellent agreement for the LBA-inner array with the numerical results computed in realistic electrical and geometrical conditions. On the other hand, a similar comparison for the LBA-outer array suffers for the UAV flying in the NF region of the array.

Data Availability

The raw data and plots supporting the conclusions of the study are available on demand from the corresponding author.

Conflicts of Interest

The authors declare that they have no conflicts of interest.

Acknowledgments

This work was supported in part by the National Institute for Astrophysics under program TECNO INAF 2014 and in part by the Netherlands Organization for Scientific Research.

References

- [1] P. E. Dewdney, P. J. Hall, R. T. Schilizzi, and T. J. L. W. Lazio, "The square kilometre array," *Proceedings of the IEEE*, vol. 97, no. 8, pp. 1482–1496, 2009.
- [2] M. P. van Haarlem, M. W. Wise, A. W. Gunst et al., "LOFAR: the low-frequency array," *Astronomy & Astrophysics*, vol. 556, p. A2, 2013.
- [3] W. A. van Cappellen, S. J. Wijnholds, and J. D. Bregman, "Sparse antenna array configurations in large aperture synthesis radio telescopes," in *2006 European Radar Conference*, pp. 13–15, Manchester, UK, 2006.
- [4] S. J. Wijnholds, "LOFAR configuration considerations as a design exercise for SKA," in *SKA Memo Series, no. 143*, p. 76, Square Kilometer Array, 2012.
- [5] D. Gonzalez-Ovejero, E. de Lera Acedo, N. Razavi-Ghods, C. Craeye, and L. E. G. Munoz, "Non-periodic arrays for radio-astronomy applications," in *2011 IEEE International Symposium on Antennas and Propagation (APSURSI)*, pp. 1762–1765, Spokane, WA, USA, 2011.
- [6] G. Virone, P. Bolli, F. Paonessa et al., "Strong mutual coupling effects on LOFAR: modeling and in situ validation," *IEEE Transactions on Antennas and Propagation*, vol. 66, no. 5, pp. 2581–2588, 2018.
- [7] G. Virone, A. M. Lingua, M. Piras et al., "Antenna pattern verification system based on a micro unmanned aerial vehicle (UAV)," *IEEE Antennas and Wireless Propagation Letters*, vol. 13, pp. 169–172, 2014.
- [8] P. Bolli, G. Pupillo, F. Paonessa, G. Virone, S. J. Wijnholds, and A. M. Lingua, "Near-field experimental verification of the EM models for the LOFAR radio telescope," *IEEE Antennas and Wireless Propagation Letters*, vol. 17, no. 4, pp. 613–616, 2018.
- [9] W. A. Van Cappellen, J. D. Bregman, and M. J. Arts, "Effective sensitivity of a non-uniform phased array of short dipoles," *Experimental Astronomy*, vol. 17, no. 1–3, pp. 101–109, 2004.
- [10] W. A. van Cappellen, M. Ruiter, and G. W. Kant, "Low band antenna-architectural design document," ASTRON technical report, 2007-03-21, 2007.
- [11] P.-S. Kildal, "Equivalent circuits of receive antennas in signal processing arrays," *Microwave and Optical Technology Letters*, vol. 21, no. 4, pp. 244–246, 1999.
- [12] C. A. Balanis, *Antenna Theory—Analysis and Design*, John Wiley & Sons, 2nd edition, 1997.
- [13] H. L. van Trees, *Optimum Array Processing: Part IV of Detection, Estimation, and Modulation Theory*, John Wiley & Sons, New York, NY, USA, 2002.
- [14] S. Pivnenko, J. E. Pallesen, O. Breinbjerg et al., "Comparison of antenna measurement facilities with the DTU-ESA 12 GHz validation standard antenna within the EU Antenna Centre of Excellence," *IEEE Transactions on Antennas and Propagation*, vol. 57, no. 7, pp. 1863–1878, 2009.
- [15] G. Pupillo, G. Naldi, G. Bianchi et al., "Medicina array demonstrator: calibration and radiation pattern characterization using a UAV-mounted radio-frequency source," *Experimental Astronomy*, vol. 39, no. 2, pp. 405–421, 2015.
- [16] P. Bolli, G. Pupillo, G. Virone et al., "From MAD to SAD: the Italian experience for the LOW-frequency aperture array of SKA1-LOW," *Radio Science*, vol. 51, no. 3, pp. 160–175, 2016.



Hindawi

Submit your manuscripts at
www.hindawi.com

